Visual Abstract

Damage assessment of different FDM-processed materials adopting Infrared Thermography

Danilo D'Andrea, Giacomo Risitano, Marcello Raffaele, Filippo Cucinotta, Dario Santonocito
University of Messina, Italy
danilo.dandrea@unime.it, http://orcid.org/0000-0002-9809-8434
giacomo.risitano@unime.it, http://orcid.org/0000-0002-0506-8720
marcello.raffaele@unime.it, http://orcid.org/0000-0003-0638-1919
filippo.cucinotta@unime.it, http://orcid.org/0000-0002-0304-4004
dsantonocito@unime.it, http://orcid.org/0000-0002-9709-9638

ABSTRACT. The use of components obtained through the additive manufacturing (AM) technique has become increasingly widespread in recent years, playing a central role in industrial production, and in particular in some fields such as automotive, biomedical, aerospace and electronics. Among all AM techniques, FDM (Fused Deposition Modelling) represents the most used printing technique to produce polymeric and composite components, thanks to the flexible printing process, the low cost and the diversity of the materials adopted. The aim of the present work concerns the comparison between the mechanical properties of three plastic materials printed with the FDM technique (polylactic acid PLA, polyethylene terephthalate glycol-modified PETG and Acrylonitrile-butadiene-styrene ABS) using an Original Prusa i3 MK3S, by varying the raster angle between 0°, 45° and 90° degrees. Infrared Thermography has been adopted to monitor the temperature evolution during static tensile tests and to assess stress level that can initiate damage within the material. Failure analysis was performed to correlate the mechanical behaviour with the microstructural characteristics of the materials.

KEYWORDS. 3D printing; DfAM; Microstructure; PLA; ABS; PETG.

OPEN ACCESS

Citation: D'Andrea, D., Risitano, G., Raffaele, M., Cucinotta, F., Santonocito, D., Mechanical behaviour and damage assessment of several FDM materials adopting infrared thermography, Frattura ed Integrità Strutturale, 62 (2022) 75-90.

Received: 16.06.2022
Accepted: 15.07.2022
Online first: 30.07.2022
Published: 01.10.2022

INTRODUCTION

The design and realization of 3D printing objects through Additive Manufacturing (AM) technique has become increasingly popular in the last years [1–3]. The growing trend is related to the fact that this technique allows to manufacture components of complex geometry without removing material with several advantages compared with conventional manufacturing processes [4–6]. Moreover, with respect to conventional techniques, such as cutting, casting and turning, the waste of raw material is reduced. The idea at the basis of this technique is to realize a component through filament/powder of material deposited layer by layer. Additive manufacturing plays an increasingly central role in industrial production, and in particular in some fields such as automotive [7], biomedical [8–10], aerospace [11] and electronics [12].

Thanks to the evolution of rapid prototyping, interest has grown in the design of topologically optimized components [13], due to the development of algorithms such as the stochastic methods [14] or the hollowing method [15], allow to maintain good mechanical characteristics by reducing their weight, this last parameter is fundamental in light structures. A lot of printing method are commercially available, such as Fusion Deposition Modelling (FDM) [16], Laminated Object Manufacturing (LOM), Stereolithography (SL) [17], Powder-Bed Fusion [18], Selective Laser Sintering (SLS) [19], and Electron Beam Melting (EBM) [20,21]. Among all the techniques, the FDM represents the most used printing technique to produce polymer and composite components [22], thanks to the flexible printing process, low cost, and diversity of materials used. To obtain a component by FDM, a 3D model must be established and imported into slicing software setting all printing parameters such as printing speed, layer thickness, filling speed and printing temperature to control the 3D printing machine [23]. During the modelling process, a filament is heated and extruded into the nozzle in a semi-liquid state and deposited on the previous material layer, repeating the process until the object is completely made [24]. Considering the printing principle of the FDM technique, it is reasonable to consider materials having orthotropic properties. In particular, the mechanical properties in the direction perpendicular to the material layer are different from those in the transverse plane. There are many studies in the literature that address the problem of the printing angle. Zhao et al [25] proposed two novel theoretical models to predict the tensile strength and Young's modulus of FDM additive manufacturing PLA (polylactic acid) material with different printing angles and layer thicknesses. Firstly, the strength theoretical model is established based on the transversely isotropic material hypothesis and Tsai-Hill strength criterion. Then, Young's modulus theoretical model is established based on the orthotropic material hypothesis under plane stress state. Yao et al.[26] studied a new separate-modes of transversely isotropic theoretical failure model to predict the tensile failure strength and separation angle of FDM 3D printing PLA material based on the hypothesis of transverse isotropy and the classical separate-modes failure criterion. The tensile specimens designed were fabricated at 7 different printing angles (0°, 15°, 30°, 45°, 60°, 75°, 90°) and three levels of printing layer thickness (0.1 mm, 0.2 mm, 0.3 mm). Djouda et al. [27] performed an experimental study on FDM by adopting Digital Image Correlation to assess the local strain behaviour in the proximity of notches. Due to the several thermal cycles to which the material is subjected during the FDM printing process, structural integrity must be monitored to ensure reliable devices [28]. Among non-destructive techniques for structures reliability, thermography has a prominent role due to its easy-to-use and rapidity in providing results. In the last thirty years, it has been applied to a large class of materials by the Risitano's Research Group and other researchers around the world [29–32]. More recently, Risitano and Risitano [33], by observing the temperature evolution during a static tensile test on specimen, correlated the deviation from the linear thermoelastic law to the onset of irreversible damage within the material. They linked the corresponding applied macroscopic stress to a "limit stress" that, if cyclically applied, will lead the material to fatigue failure.

The focus of the present work concerns the comparison between the mechanical properties of three plastic materials printed with FDM technique (polylactic acid PLA, polyethylene terephthalate glycol-modified PETG and Acrylonitrile-butadiene-styrene ABS), varying the raster angle between 0°, 45° and 90° degrees. Infrared Thermography has been adopted to monitor the temperature evolution during static tensile tests and to assess stress level that can initiate damage within the material. Failure analysis was performed to correlate the mechanical behaviour with the microstructural characteristics of the materials. The findings are of interest in the field of Design for Additive Manufacturing (DfAM) [34], allowing designers to orient themselves in the choice of the best materials and printing parameters in function of their needs and to understand and forecast the ways of failure.

THEORETICAL BACKGROUND: ENERGY RELEASE DURING A STATIC TENSILE TEST

In the last thirty years, infrared thermography has been applied to monitor the temperature evolution during fatigue tests of common engineering materials. The first researcher that observed the temperature trend of a cyclically loaded material was Risitano in 1986 [35]. In 2000, La Rosa and Risitano [36] proposed a rapid procedure to assess the fatigue limit of the material by monitoring the energy release of material loaded with a stress level above its fatigue limit. The Risitano's Thermographic Method (RTM) allows to assess in a few hours and with a very limited number of specimens the fatigue limit of the material and its SN curve [37].

Lord Kelvin [38] in 1853 discovered the thermoelastic effect of solid materials. The temperature law of variation of a solid material under uniaxial tensile stress can be expressed as (Eqn. 1):

$$\Delta T = -K_m T_0 I_\sigma \tag{1}$$

where K_m is the thermoelastic coefficient of the material, T_0 the initial temperature of the material and I_σ the first invariant of the stress tensor. Caglioti et al. [39] studied the thermoelastic effect defining a temperature vs. time diagram for a steel

specimen during a monoaxial tensile test. The main aim was to determine the yield strength of the material as the corresponding stress at which the temperature signal exhibits a minimum value, with a horizontal tangent. Melvin et al. [40,41] performed studies on the heat generated during a monoaxial tensile test of steel and related the formation of microcracks with the loss of linearity of the temperature signal in time.
By observing the temperature trend during a static tensile test, it is possible to distinguish three different phases (Fig. 1). In the first phase (Phase I), all the material is elastically stressed, and the temperature shows a linear trend. As the applied stress is increased, some damage within the material is introduced. The material has some microplastic area; however, it is mainly elastically stressed (Phase II). In such phase, the temperature signal shows a deviation from the first linear elastic trend (point A). By increasing the applied stress level, the temperature signal reaches a plateau region (point B), then irreversible plastic deformations have a predominant role and the temperature begins to increase up to the failure of the material (Phase III).

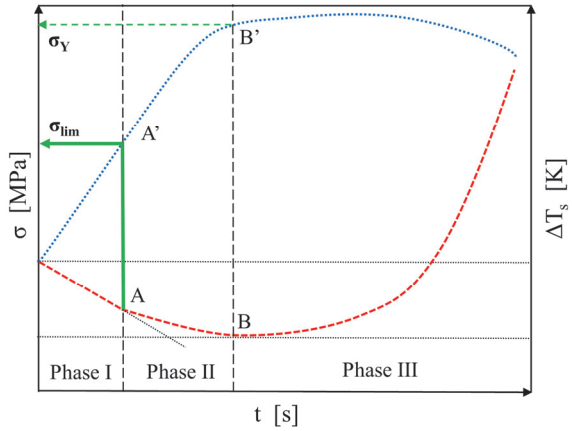

Figure 1: Qualitative ΔT_s trend vs machine time (t) vs applied stress (σ).

Melvin and co-workers evaluated the entropy of the phenomena and obtained the expression of the temperature variation for a cylindrical specimen made of homogeneous material and subjected to a constant stress rate (stress over time), with σ_m the average stress in the specimen's cross section:

$$\Delta T=-K_m T_0 \sigma_m -B\frac{\sigma_m^2}{3c_v E} \quad (2)$$

Such mathematical expression is not easy to apply in practical cases due to the difficulty in assessing some parameters (for example B is the drag coefficient, strictly related to the Burges vector b). The first term of Eqn. 2 is related to the linear elastic part, while the second term is related to the plastic one. In this analytical model, the loss of linearity in the temperature vs. time signal (ΔT-t) occurs at the first micro-plasticity, which occurs before yielding as verified by numerous experimental tests.
Thanks to infrared thermography it is possible to monitor the specimen's surface temperature during a monoaxial tensile test and obtain temperature vs. stress vs. time diagrams [42]. In such diagrams it is possible to define the stress level at which the temperature deviates from the linear trend, the limit stress σ_{lim} [33] (point A, Fig. 1). Adiabatic test conditions are required to prevent the specimen to exchange heat with the surrounding environment, so the test velocity must be chosen accordingly. The limit stress coincides with the macro stress value able to produce micro-cracks within the material and, if cyclically applied, its fatigue failure.

MATERIALS AND METHODS

FDM specimen preparation

The geometry of the specimen was realized according to Type I of the ASTM D638 standard (Fig. 2a). All specimens were produced by an Original Prusa i3 MK3S + FDM printer (Prusa Research, Prague, Czech Republic) equipped with a brass nozzle 0.4 mm in diameter. The slicing was done with the software PrusaSlicer 2.4.0 (Prusa Research,

Prague, Czech Republic). The filaments studied were ABS, PETG and PLA from Sunlu producer (1.75±0.02 mm of diameter). On the extruder head there are two counter-rotating driving wheels that pull the filament and push it through a heating block and a hot nozzle. A tube made of polytetrafluorethylene (PTFE) guides the filament to the extruder unit. The unit also includes a sensor, which detects the incoming filament. FDM technology is based on the deposition of a plastic filament according to a precise sequence of instructions showing the displacement coordinates of the x, y, z axes of the 3D printer. These instructions are provided by a special file created by a slicing software that reconstructs the object one level at a time on the construction plane. After the material was molten, the FDM printer deposited a strand by moving the printing head according to the predefined geometry. This occurred in a layer-by-layer manner. After finishing the first layer, the height of the extrusion head was increased by the amount of one layer and the second layer was deposited. This process was repeated until a defined height of the geometry was reached. The used processing parameters are summarized in Tab. 1. Nozzle and build platform temperatures were chosen for each material to match the producer's material data sheet. To avoid further influences of different processing parameters, such as layer thickness, temperature, infill percentage, infill pattern, or printing speed on the mechanical properties, these were kept constants for all specimens produced in this study (Tab. 1). The printing infill was set to 100% to achieve the highest mechanical properties.

Parameters	ABS	PETG	PLA
Nozzle temperature [°C]	260	240	200
Bed temperature [°C]	90	90	90
Adhesion	Brim	Brim	Brim
Layer thickness [mm]	0.15	0.15	0.15
Printing speed [mm s^{-1}]	60	60	60
Printing infill [%]	100	100	100

Table 1: Processing parameters of ABS, PETG and PLA.

Three different print orientations were chosen for the filling. The approach used consists of positioning the geometries of the three specimens, already oriented in the three angles considered (0°, 45° and 90°) and setting a single filling angle in the FDM, i.e., 0 °. Fig. 2b shows the orientation of the specimens with the relative infill.

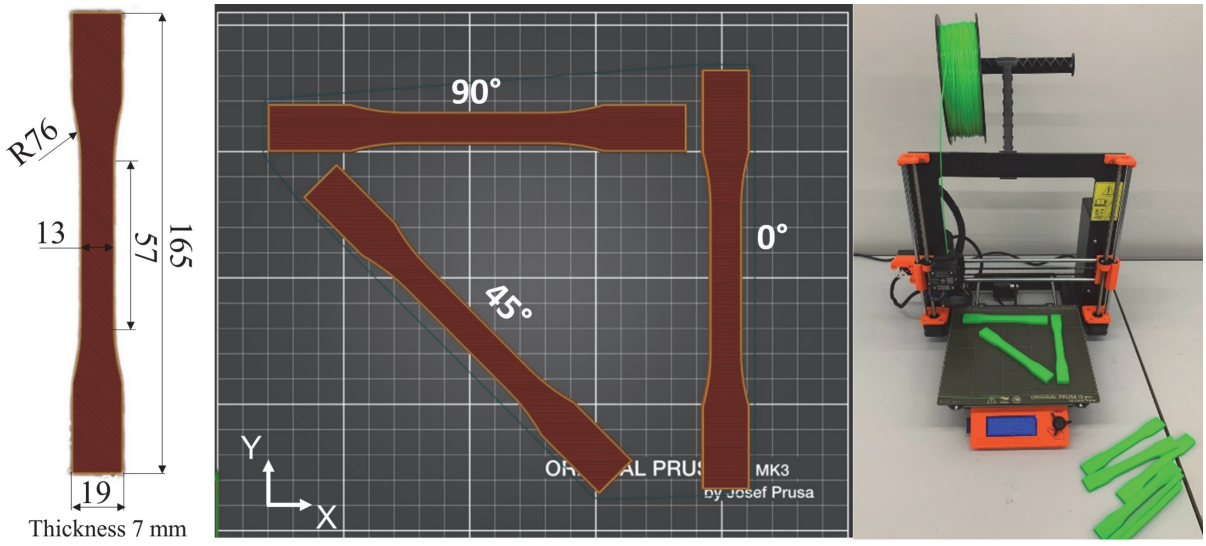

(a) (b) (c)

Figure 2: a) Orientation of the specimens with relative infill; b) Original Prusa i3 MK3S+, spool of filament and specimens.

This type of approach made it possible to obtain a faster production speed of the specimens. Each set of specimens was printed in the same ambient conditions (external temperatures, humidity). Fig. 2c shows the FDM printing setup consisting of Original Prusa i3 MK3S+, spool of filament and specimens.

Static tensile tests

The specimens were tested under displacement control, with an elongation rate of 5 mm/min, adopting a servo-hydraulic loading machine ITALSIGMA 25 kN (Fig. 3). The tests were performed at an ambient temperature and relative humidity, respectively, of 23°C and 50%. For each material and each raster angle orientation, a number of 3 specimens was tested. The strain was measured by adopting an extensometer with an initial gauge length of L_0= 50 mm.

From the static tensile tests, the engineering stress-strain curve, the Young's Modulus (E), the ultimate strength (σ_U) and the ultimate strain (ε_U) for each material were evaluated. The engineering stress was obtained as the ratio between the instantaneous force and the nominal cross-section area of the specimen, while the engineering strain was estimated as the ratio of the instantaneous elongation and the initial gauge length of the extensometer. Young's Modulus was estimated as the linear regression of the stress vs. strain between the strain levels of ε_1= 0.0005 e ε_2= 0.0025 according to the ISO527 standard. The ultimate strength and strain were evaluated as the values at failure of the specimen.

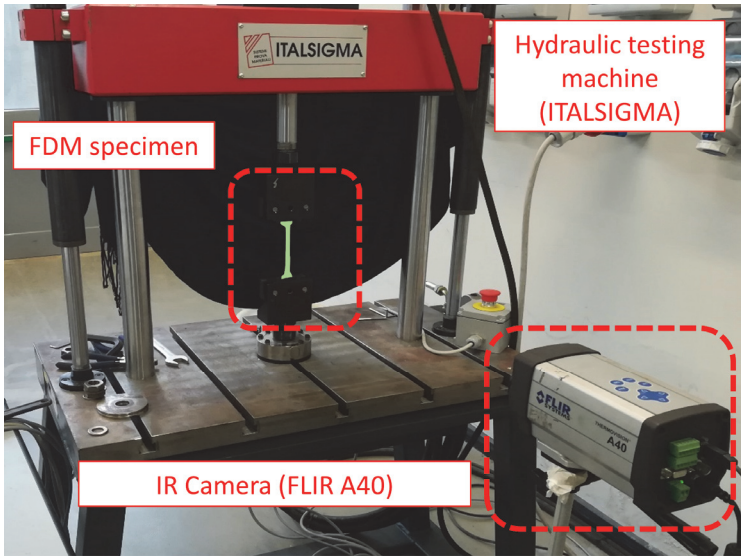

Figure 3: Experimental test setup.

During static tensile tests, the surface temperature evolution was monitored with an infrared camera FLIR A40 with an image resolution of 320x240 pixel, thermal sensitivity of 0.08 °C at 30°C and frame rate of 1 Hz. The specimens' surface was painted with black paint to increase thermal emissivity up to 0.98. The maximum temperature value of a rectangular area placed on the specimen's length has been acquired.

The evaluation of the fracture surface of the printed materials was performed using optical microscopy.

RESULTS AND DISCUSSION

Mechanical behaviour of FDM material

Static tensile tests have been performed on three different plastic materials (ABS, PETG and PLA) obtained by FDM. Three raster angle orientations have been investigated (0°, 45° and 90°) by testing three specimens for each raster angle. The engineering stress-strain curves of the materials have been obtained and reported in Fig. 4 for all the tested specimens. The ABS stress-strain curves (Fig. 4a) exhibit an almost linear trend followed by a very short hardening region before the specimen's failure. The specimens with a raster angle orientation of 0° (blue curves, Fig. 4a) have the worst mechanical performance; indeed, the plane orientation is perpendicular to the loading direction, leading to a premature failure of the specimens. The specimens with a raster angle orientation of 45° (red curves, Fig. 4a) have better mechanical performance respect to the 0° configuration. Indeed, the plane orientation is at 45° respect the loading direction, inducing

a failure mechanism governed by shear. The 90° raster angle configuration (black curves, Fig. 4a), where the planes are parallel to the loading direction, shows the best mechanical performances for the ABS specimens.

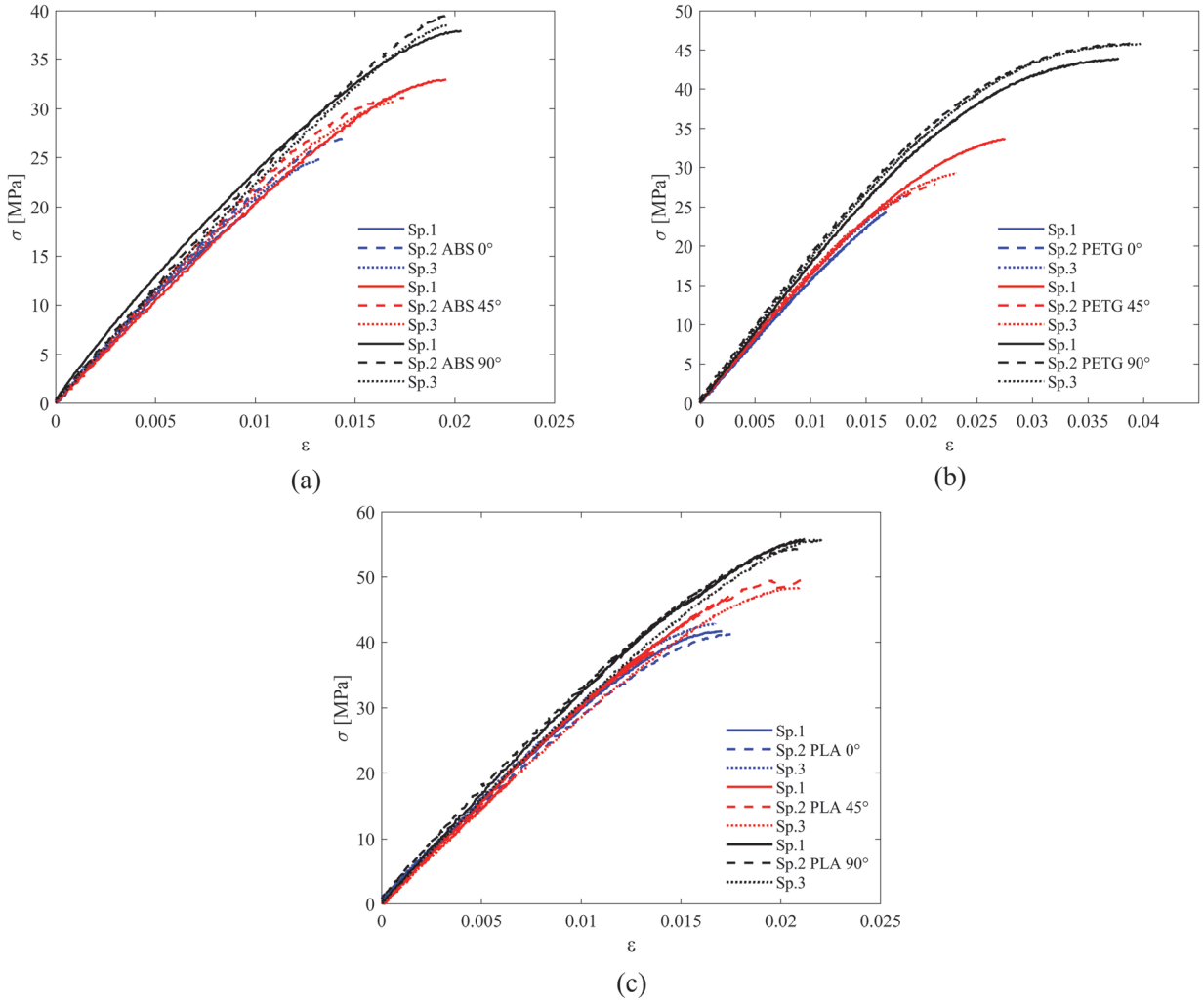

Figure 4: Engineering Stress-Strain curves at several raster angles for: a) ABS; b) PETG; c) PLA.

The PETG specimens, compared to the ABS ones, show a more marked hardening region, except for the 0°-oriented configuration (blue curves, Fig. 4b) which exhibits a brittle fracture behaviour. On the other hand, the 45°- and 90°-oriented specimens (red and black curves, Fig. 4b) have better mechanical performances. As for the ABS 0°-oriented specimens, the plane orientation respects the loading direction has a predominant role in the mechanical behaviour of the material. PLA specimens (Fig. 4c), as the previous material, show a marked mechanical behaviour strictly dependent on the raster angle orientation. This material also exhibits a hardening region, even for 0° raster angle orientation. However, the 90°-oriented has the best mechanical performances, compared to 0° and 45°, due to the parallel orientation of the plane respect to the loading direction.

Comparison of mechanical properties

From the engineering stress-strain curves of the different materials, it has been possible to evaluate the mechanical properties such as Young's Modulus, ultimate tensile strength, and ultimate strain. The average values, estimated on three specimens per material type, with one standard deviation band have been reported in Fig. 5 respect to the raster angle.

The ABS Young's Moduli have intermediate values compared to the PETG and PLA specimens, with an average value of 2276±39 MPa for 0°, 2190±65 MPa for 45° and 2403±181 MPa for 90°. The higher the raster angle orientation, the higher the standard deviation. The highest value of Young's Modulus has been reached for the 90° raster angle orientation, with fibres aligned to the loading direction. PETG has the lowest value of Young's Modulus, with a minimum value at 0°

(1633±38 MPa). The 90°-oriented specimens have the highest value (1803±5 MPa) with a smaller standard deviation compared to the 45°-oriented specimens (1727±28 MPa). PLA specimens have the highest Young's Modulus compared to the other materials (3021±127 MPa for 0°, 3161±102 MPa for 45°, 2556±254 MPa).

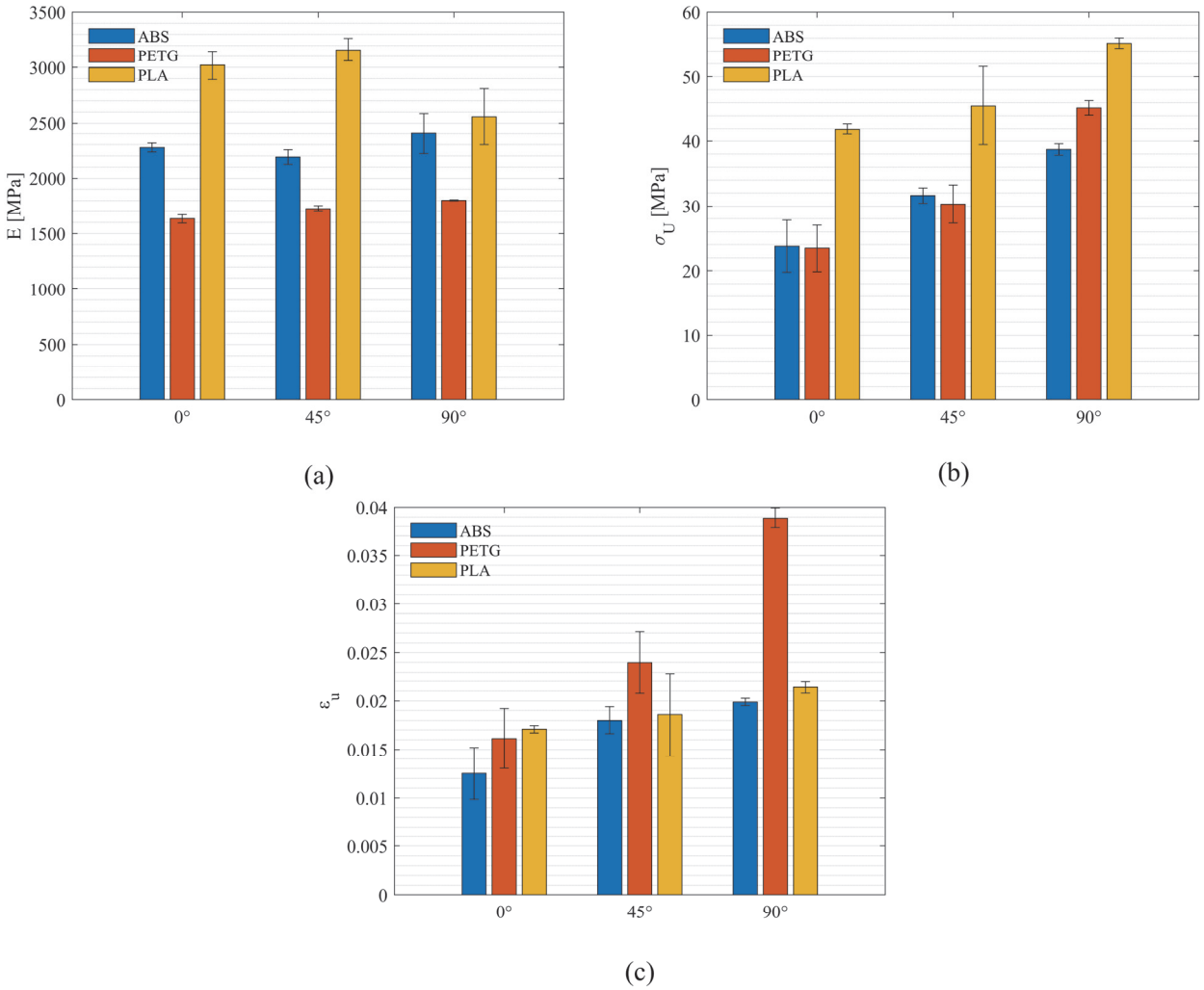

Figure 5: Comparison between mechanical properties of ABS, PETG and PLA: a) Young's Modulus; b) Ultimate strength; c) Ultimate strain.

The ultimate tensile strength of PLA specimens (Fig. 5b) is the highest compared to the ABS and PETG specimens in each raster angle orientation (41.9±0.8 MPa for 0°, 45.5±6.1 MPa for 45°, 55.2±0.8 MPa for 90°). However, a large scatter is present in the 45°-oriented specimens. ABS and PETG specimens have a comparable ultimate tensile strength (ABS: 23.8±4 MPa for 0°, 31.6±1.2 MPa for 45°, 38.7±0.9 MPa for 90°) even if in the 90° direction PETG has a higher ultimate tensile strength (PETG: 23.4±3.6 MPa for 0°, 30.3±3.0 MPa for 45°, 45.2±1.2 MPa).
Regarding the ultimate strain (Fig. 5c), PETG shows higher values as the raster angle is increased (0.01611±0.0031 for 0°, 0.02398±0.0032 for 45°, 0.03888±0.00103 for 90°). ABS and PLA specimens do not show significative differences, except for the 0°-oriented specimens (ABS: 0.01254±0.0026 for 0°, 0.017998±0.001385 for 45°, 0.01988±0.00038 for 90°; PLA: 0.01709±0.00038 for 0°, 0.01857±0.0043 for 45°, 0.0213±0.0005735 for 90°). A large scatter of the data is present in the 0° direction for ABS and PETG specimens and in the 45° direction for PETG and PLA specimens.
The above results confirm the strong anisotropy of the 3D printed specimens with mechanical properties severally dependent on the printing orientation compared to the loading direction. Dawoud et al. [43] investigate the mechanical behaviour of ABS specimens obtained by injection moulding and FDM technique. The main parameters considered were the air gap and the raster angle. Injection moulded specimens had a higher density compared to the FDM ones. This has

been addressed to the pressure settled during the injection moulding process, which compensates for the material shrinkage and reduces the air gap. Indeed, with only positive raster gap, raster touch only along one line, while with positive and negative raster angles the rasters overlap and the adjacent filaments are induced to squeeze, so this can enhance the tensile strength of the material. For injection moulded specimens they report an ultimate tensile strength of 37.7 MPa, while for FDM specimens 34.3 MPa was obtained for a positive-negative raster angle configuration of ±45°. As main observation, they report that the mechanical strength was improved when the subsequent layers are bonded with a negative raster angle, where more bonding sites by fused deposition are created. The findings of the present study are in agreement with the finding of Ziemian et al. [44], where the 90° raster angle has the highest mechanical performance, while the 0° raster angle has the lowest one. Rodriguez-Panes et al. [45] performed a comparative analysis on ABS and PLA specimens manufactured via FDM with ±45° raster angle orientation and different infill percentages. A higher infill percentage leads to better mechanical performances, however they are lower than the pure filament tested. Samykano et al. [46], by testing ABS specimens obtained by FDM, found that the optimum parameters for 3D printing using ABS are 80% infill percentage, 0.5 mm layer thickness, and 65° raster angle. The obtained ultimate tensile strength, Young's Modulus and ultimate strain are respectively 31.57 MPa, 774.50 MPa, 0.094. These values are coherent with the ones obtained in the present work and they are within the range of 45° and 90° raster angle orientation.
Srnivasan et al. [47] investigated the mechanical properties of PETG specimens obtained by FDM with different infill densities. They had shown how the best mechanical performances (ultimate tensile strength 32.12 MPa) were obtained with an infill density of 100%.

Energy release during static tensile tests

During the static tensile tests, the specimen's superficial temperature evolution has been monitored to assess possible deviation from the linear thermoelastic law.

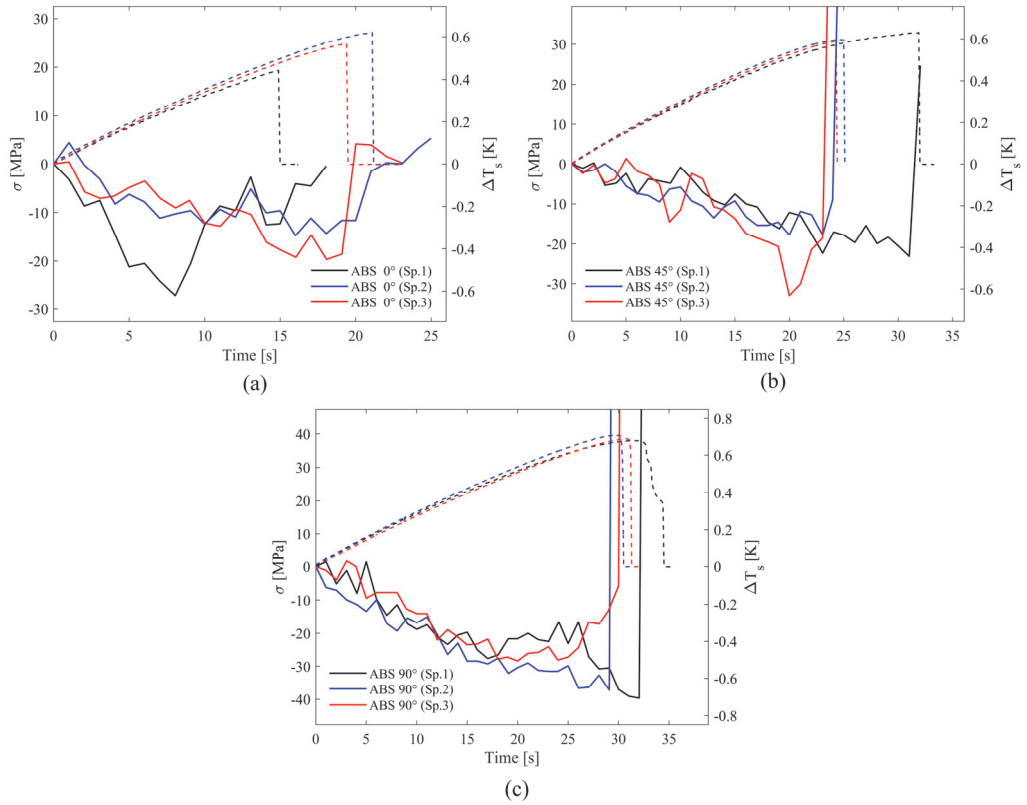

Figure 6: Energy release of ABS specimens during static tensile test with different raster angle: a) 0°; b) 45°; c) 90°.

The maximum value of temperature of a rectangular spot placed on the specimen's gauge length has been evaluated (continuous line) and plotted versus the applied stress level (dashed lines) and test time (Fig. 6, Fig. 7 and Fig. 8). The

temperature signal has been referred to the relative value respect to the beginning of the test, i.e. when the specimen is unloaded.

Fig. 6 reports the temperature evolution for ABS specimens at different raster angle orientations. The temperature signal for the 0°-oriented specimens (Fig. 6a) shows a decrement with a noisy signal, with relevant differences among each of the three tested specimens. It is difficult to assess the two temperature phases and the third phase is not present due to a sudden failure of the specimens. The temperature signal of 45°-oriented specimens (Fig. 6b) is characterized by a marked linear decrement followed by a sudden failure of the specimens with a very high temperature increment. The 90°-oriented specimens (Fig. 6c) have a clear temperature trend compared to the previous raster angle orientations. A slight change in the slope of the temperature signal can be identified between 17 s and 20 s. After Phase II, the specimens experience a sudden failure with a high temperature increment.

PETG 0°-oriented specimens (Fig. 7a) show a very noisy temperature signal without any significative temperature increment at failure. On the other hand, the 45°-oriented specimens (Fig. 7b) exhibit a linear decrement up to the sudden specimen's failure, with a relevant temperature increment. Regarding the 90°-oriented specimens (Fig. 7c), it is clearly possible to distinguish the two temperature phases, followed by a sudden failure of the specimens with high temperature increment. The transition between Phase I and Phase II can be identified within 40÷45 s time interval.

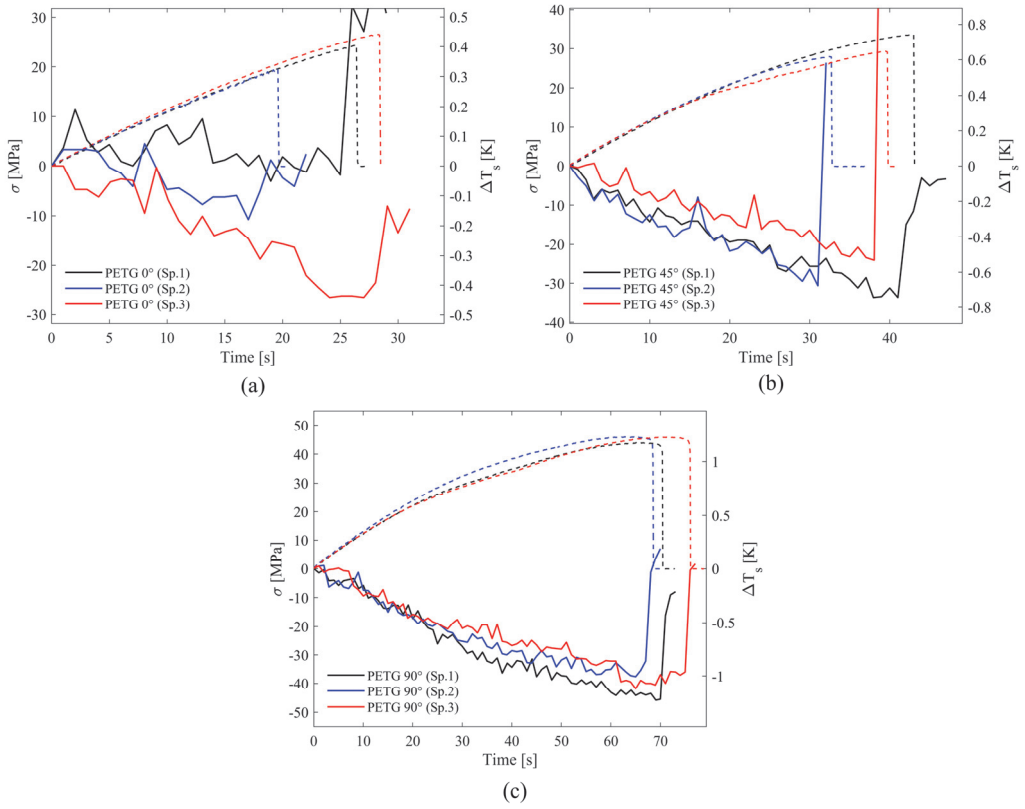

Figure 7: Energy release of PETG specimens during static tensile test with different raster angle: a) 0°; b) 45°; c) 90°.

PLA specimens with 0° raster orientation (Fig. 8a) have a clear temperature signal, however they show an almost linear decrement up to the sudden failure of the specimen. On the other hand, the 45°-oriented specimens (Fig. 8b) have a clear distinction between Phase I and Phase II but followed by a sudden failure of the specimens with the highest temperature decrement respect to the other materials analysed (about -1 K). The same observation applies to the 90°-oriented specimens but without a clear distinction between the two phases.

For those specimens that has shown a clear distinction between Phase I and Phase II (ABS 90°, PETG 90° and PLA 45°), it has been possible to assess the value of the limit stress by performing the intersection of two straight lines related to the temperature signal. As in the previous analysis, the temperature signal has been reported versus the applied stress level and time. In this case, to enhance the linear elastic trend and to neglect some possible outliers, the temperature signal has been filtered with a *rlowess* filter with a data span of 5%, then it has been divided into two different temperature sets. The first

temperature set (ΔT_1) is related to the first linear thermoelastic temperature trend (Phase I), while the second set is related to Phase II (ΔT_2), where the variance to the linearity has been noticed, and before Phase III. The temperature points near the transition area from Phase I and Phase II have been neglected (Experimental temperature set). For sake of brevity only the analysis of a single test for material has been reported considering that the same specimens exhibit similar behaviour. The ABS 90°-oriented specimen (Fig. 9a, Specimen no. 2) exhibits a deviation from the linear elastic trend of the signal for a testing time of 16.95 s, identified by performing the intersection between the linear regression of the ΔT_1 and ΔT_2 time series. The corresponding stress level where the transition from Phase I to Phase II happen is the limit stress. For this test, it is equal to σ_{lim}= 26.4 MPa. For the three tested ABS specimens, with a raster angle orientation of 90°, an average value of the limit stress has been found to be equal to σ_{lim}= 25.3±1.1 MPa.

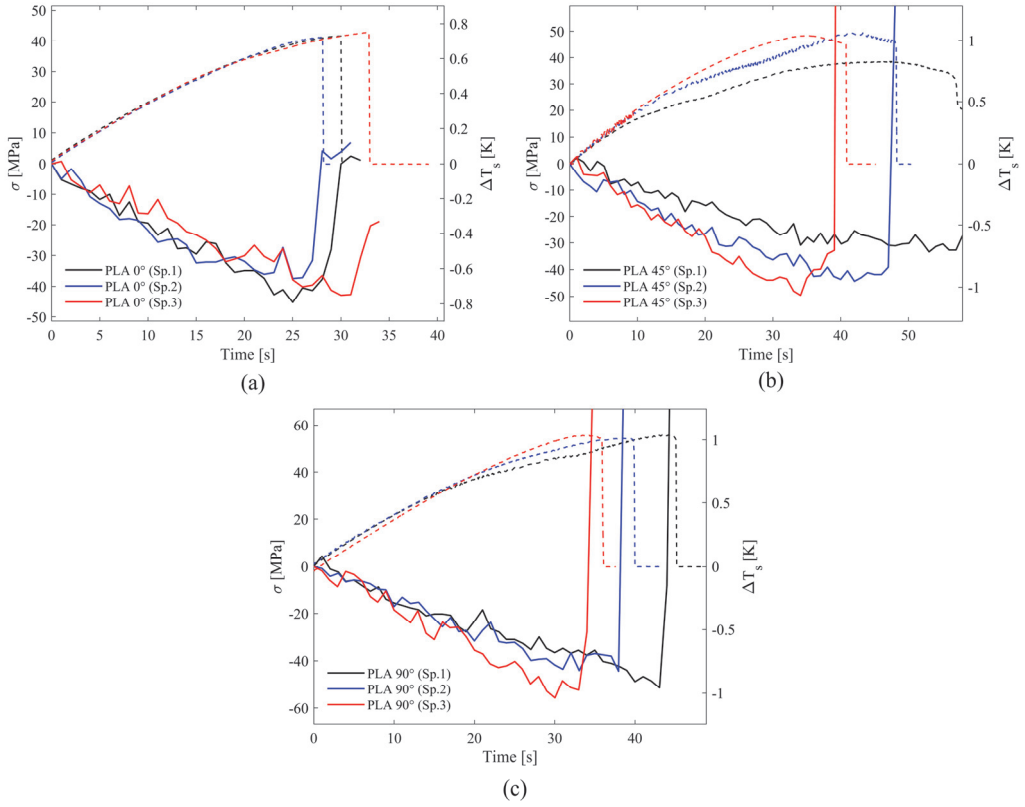

Figure 8: Energy release of PLA specimens during static tensile test with different raster angle: a) 0°; b) 45°; c) 90°.

The same procedure followed for the ABS specimens has been adopted to identify the limit stress of the PETG specimens with a raster angle orientation of 90°. Fig. 9c reports the filtered temperature trend of Specimen no. 2, where it is clearly identifiable the first linear temperature decrement followed by a second temperature decrement phase. The transition time has been identified as 32.8 s with a corresponding value of the limit stress equal to σ_{lim}= 34.4 MPa. For the PETG specimens with a raster angle orientation of 90° an average value of the limit stress has been assessed as σ_{lim}= 34.3±0.4 MPa. For the PLA specimens, the raster angle orientation that shows a transition between Phase I and Phase II has been the 45° one. Results of the test performed on Specimen no. 1 (Fig. 9c) show a value of the limit stress equal to σ_{lim}= 33.3 MPa. For the three tests performed on this PLA configuration, the average value has been σ_{lim}= 33.7±0.6 MPa.

The assessed value of the limit stress, according to the model proposed by Risitano and Risitano [33], can be related to a macroscopic stress level that, if applied cyclically, can lead to the failure of the specimen. This stress level is responsible for the activation and growth of irreversible damage within the material. Infrared thermography has been applied for the damage investigation of composites materials [48]. Santonocito [49] applying infrared thermography on 3D-printed PA12 specimens, obtained by MultijetFusion printing system, identified a limit stress for that material. Constant amplitude fatigue test performed at a stress level near the identified limit stress showed failure and run out (i.e. infinite life of the specimen) confirming those findings. Santonocito et al. [50] applying the STM on PA12, specimens obtained by Selective Laser Sintering, confirmed that the limit stress is in good agreement with the findings of the test performed according to the RTM.

Energy-based approaches have been proved to assess the fatigue properties of additive manufactured material with a limited number of specimens and in a short amount of time. To verify the correlation between the limit stress of FDM materials and their fatigue limit a traditional fatigue test campaign have to be performed in future studies.

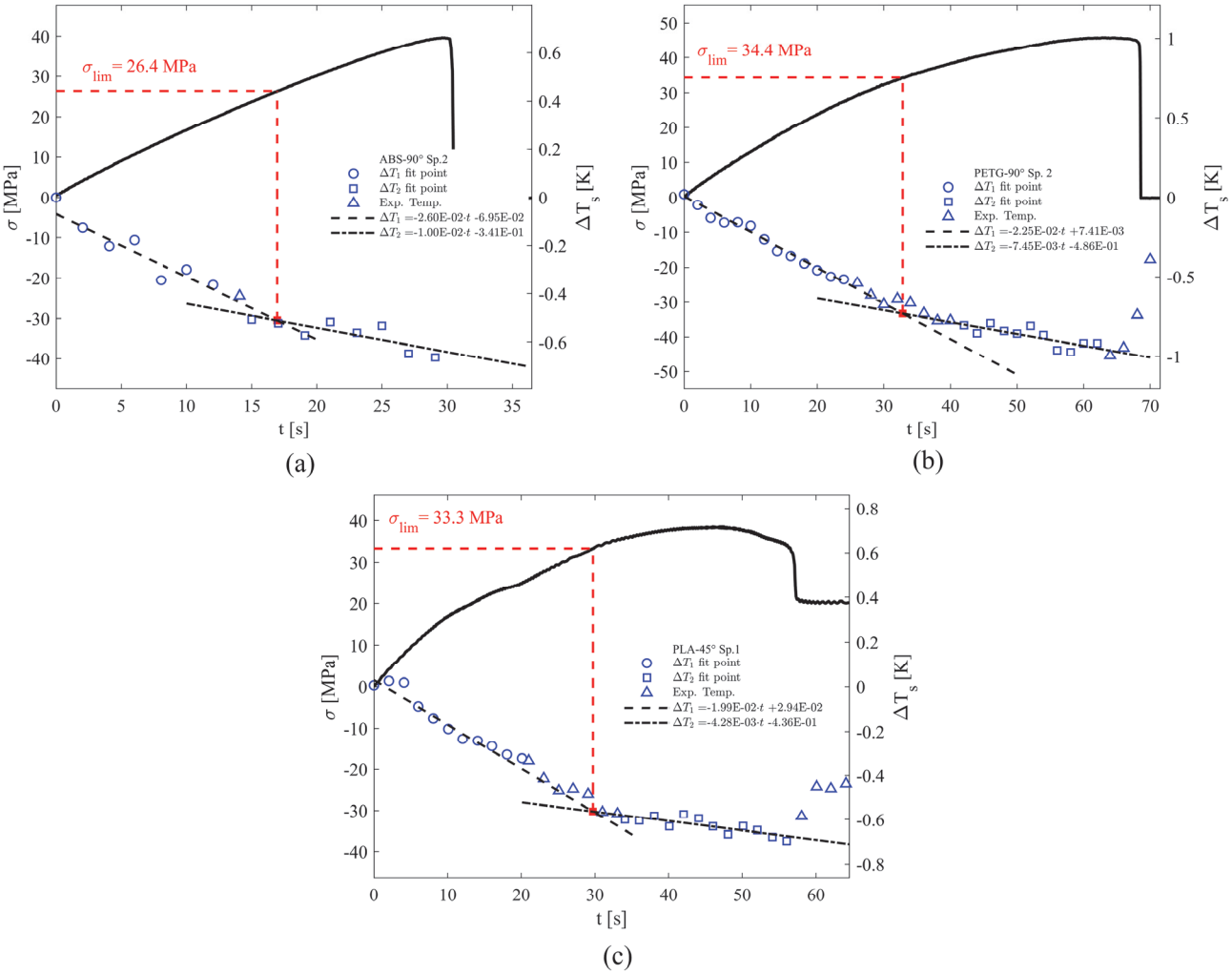

Figure 9: Limit stress assessed in: a) ABS 90°; b) PETG 90°; c) PLA 45°.

Fracture Surface

To confirm the mechanical behaviour of FDM printed materials, a failure analysis of fracture surfaces was performed. As has already been highlighted by the engineering stress-strain curves, depending on the type of material and the raster orientation, the morphology of the fracture surface also changes. It is necessary to underline that all materials analysed exhibit a brittle behaviour, as also shown in Figs. 10, 11 and 12. Analysing the fracture surfaces of the samples obtained with raster angle orientation at 0° degrees (Fig. 10), it is possible to notice a brittle behaviour, with reduced areas of plasticization, more evident in Fig. 10a in the external skin of the ABS specimen. However, it is necessary to specify that the two external layers that characterize the samples have an orientation of 90° and therefore a different behaviour. On the other hand, Fig. 10c shows a slight plasticization of the PLA sample, as evident from the lower part of the fracture surface and confirmed by the bar chart of Fig. 5.

For the samples obtained with the raster angle orientation of 45°, a fracture mechanism governed by shear is noted, which involves the formation of different fracture planes, as shown in Fig. 11. In Fig. 11a, it can be seen that ABS, in the case of 45 ° orientation, has a brittle behaviour with a fragmentation of the fracture surface in many planes. As regards PETG and PLA, on the other hand, there are large areas of plasticization with less fragmentation of the fracture surface (Fig. 11b, c).

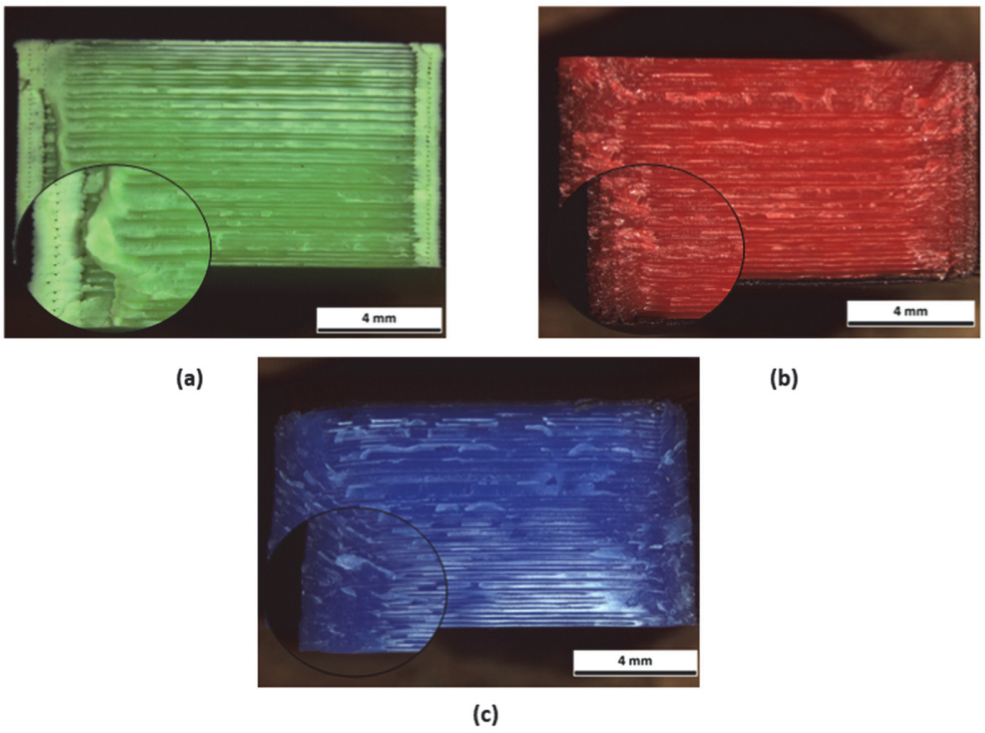

Figure 10: Fracture surfaces of raster angle 0° orientation specimens: a) ABS; b) PETG; c) PLA.

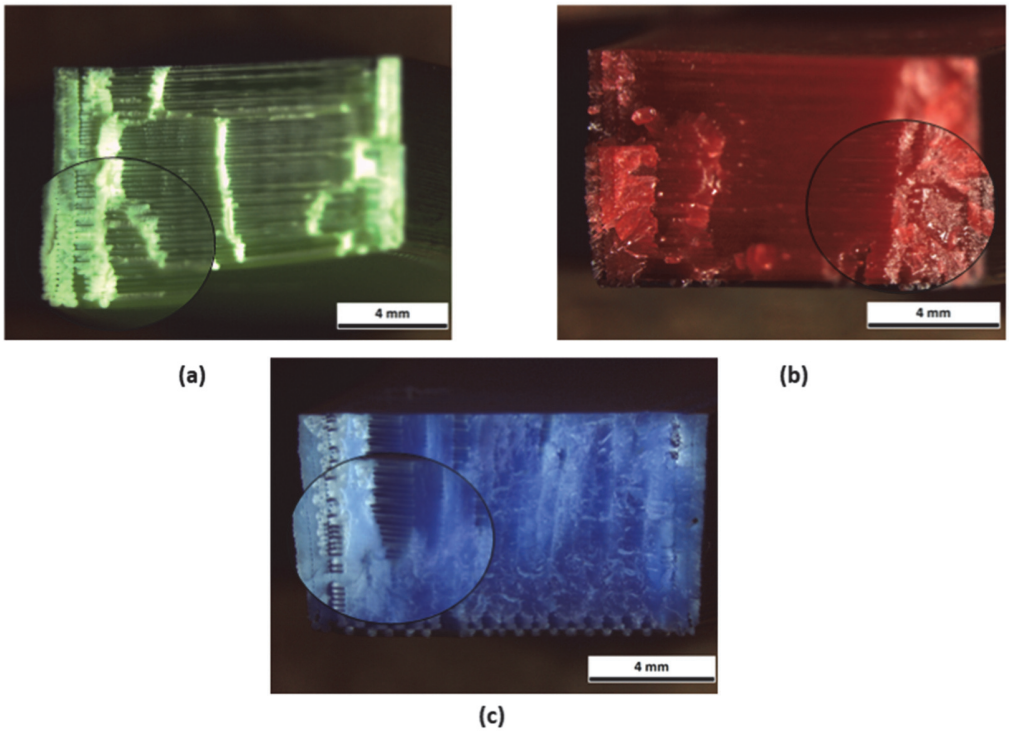

Figure 11: Fracture surfaces of raster angle 45° orientation specimens: a) ABS; b) PETG; c) PLA.

As regards the behaviour of the samples obtained with the orientation of the raster angle at 90°, is it possible to note a clearly different behaviour from the samples at 0° and 45°. First of all, since the fibres are oriented along the direction of the load, large areas of plasticization can be seen on the fracture surfaces (Fig. 12). In particular, by analysing the fracture

surface of the ABS sample (Fig. 12a), we can see a generalized plasticization of the fibres over the entire surface and a high delamination effect. Especially in the central area there is the decohesion of the fibres and the creation of large voids. Also for the PETG specimen (Fig. 12b) a large plasticization of the fibres can be highlighted as shown by the diagram in Fig. 6, but unlike ABS this is not localized over the entire fracture surface. Also for PETG a delamination of the fibres can be highlighted, but to a lesser extent than for ABS. Finally, as shown in Fig. 12c, PLA is characterized by a fracture surface with a plasticization zone and consequent delamination and void formation, and a fracture surface area with brittle behaviour and less delamination. The phenomenon of delamination and consequent formation of voids that characterizes all the samples with a raster angle orientation at 90° is due to the stretching phenomenon of the fibres which, being oriented along the load direction, undergo plasticization and decohesion.

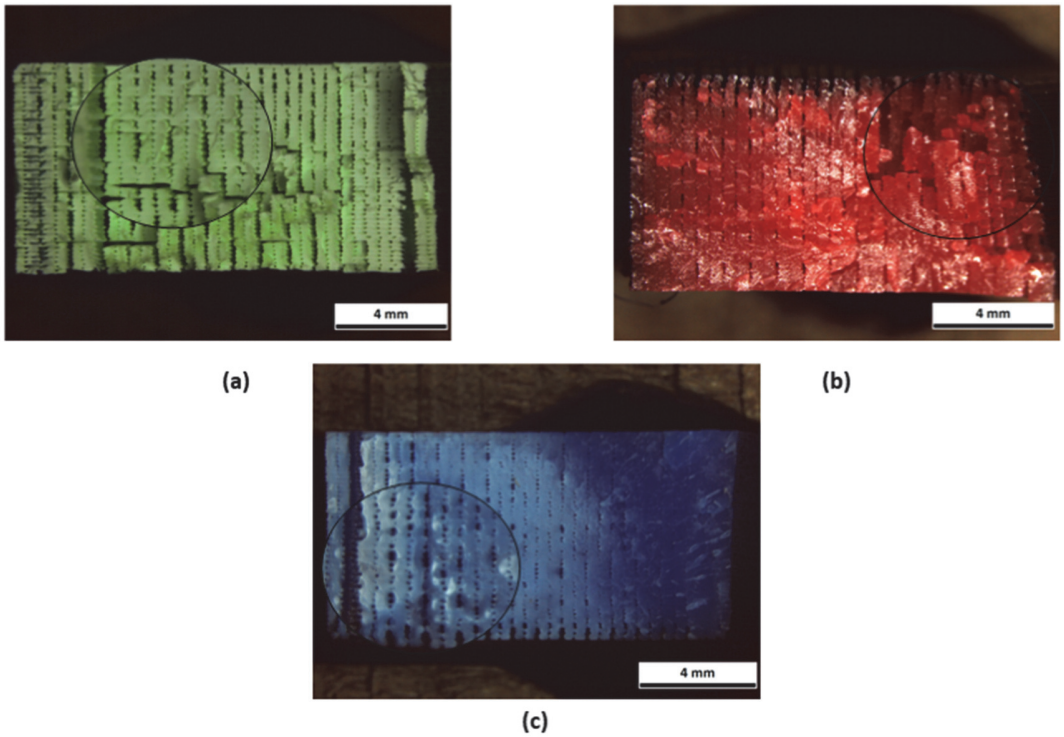

Figure 12: Fracture surfaces of raster angle 90° orientation specimens: a) ABS; b) PETG; c) PLA.

Conclusions

Static tensile tests have been performed on 3D-printed specimens obtained via Fused Deposition Modelling. The materials under study were ABS, PETG and PLA. Three different raster angle orientations have been chosen to print the specimens (0°, 45° and 90°). From the static tensile tests, the engineering stress-strain curves of the materials have been retrieved and the superficial temperature trend has been monitored with an infrared camera. The main results of the study are the following:

- The materials have linear elastic behaviour followed by a small hardening phase. The mechanical properties are strictly dependent on the raster angle orientation, with the plane perpendicular to the loading direction (0°) showing the worst mechanical performances compared to the plane parallel to it (90°). The 45°-oriented planes are more subjectable to shear failure.
- The materials show the typical trend of the linear thermoelastic law in a more marked way with 45° and 90° oriented planes. Especially, in the 90° direction it has been possible to identify two different phases of the temperature signal. The transition stress level at which the temperature signal deviates from the linearity can be related to the limit stress of the material, i.e. the first irreversible damage within it.
- A failure analysis was performed on the fracture surfaces to confirm the behaviour of the material, highlighted by the engineering curves

Further studies must be performed to correlate the limit stress with the fatigue limit of FDM material. The adoption of energy methods, as the Static Thermographic Method or Risitano's Thermographic Method, allows to obtain time and material-safe useful information regarding the fatigue life of 3D-printed materials where the mechanical and fatigue performances are severally affected by changing some printing parameters.

REFERENCES

[1] Turner, B.N., Strong, R., Gold, S.A. (2014). A review of melt extrusion additive manufacturing processes: I. Process design and modeling, Rapid Prototyp. J., 20(3), pp. 192–204, DOI: 10.1108/RPJ-01-2013-0012.

[2] Wang, X., Jiang, M., Zhou, Z., Gou, J., Hui, D. (2017). 3D printing of polymer matrix composites: A review and prospective, Compos. Part B Eng., 110, pp. 442–458, DOI: 10.1016/j.compositesb.2016.11.034.

[3] Parandoush, P., Lin, D. (2017). A review on additive manufacturing of polymer-fiber composites, Compos. Struct., 182(August), pp. 36–53, DOI: 10.1016/j.compstruct.2017.08.088.

[4] D'Andrea, D., Pistone, A., Risitano, G., Santonocito, D., Scappaticci, L., Alberti, F. (2021). Tribological characterization of a hip prosthesis in Si3N4-TiN ceramic composite made with Electrical Discharge Machining (EDM), Procedia Struct. Integr., 33, pp. 469–481.

[5] Khanna, N., Shah, P., de Lacalle, L.N.L., Rodríguez, A., Pereira, O. (2021). In pursuit of sustainable cutting fluid strategy for machining Ti-6Al-4V using life cycle analysis, Sustain. Mater. Technol., 29, pp. e00301.

[6] Gómez-Escudero, G., Jimeno Beitia, A., Martínez de Pissón Caruncho, G., López de Lacalle, L.N., González-Barrio, H., Pereira Neto, O., Calleja-Ochoa, A. (2021). A reliable clean process for five-axis milling of knee prostheses, Int. J. Adv. Manuf. Technol., 115(5), pp. 1605–1620.

[7] Böckin, D., Tillman, A.-M. (2019). Environmental assessment of additive manufacturing in the automotive industry, J. Clean. Prod., 226, pp. 977–987.

[8] Cucinotta, F., Guglielmino, E., Longo, G., Risitano, G., Santonocito, D., Sfravara, F. (2019). Topology optimization additive manufacturing-oriented for a biomedical application, 1, Springer International Publishing.

[9] Cucinotta, F., Mineo, R., Raffaele, M., Salmeri, F. (2021).Assessment of the Run-Out of an Intervertebral Cervical Cage Fabricated by Additive Manufacturing Using Electron Beam Melting. International Design Engineering Technical Conferences and Computers and Information in Engineering Conference, vol. 85376, American Society of Mechanical Engineers, p. V002T02A041.

[10] Araújo, H., Leite, M., Ribeiro, A.M.R., Deus, A.M., Reis, L., Vaz, M.F. (2019). Investigating the contribution of geometry on the failure of cellular core structures obtained by additive manufacturing, Frat. Ed Integrita Strutt., 13(49), pp. 478–486, DOI: 10.3221/IGF-ESIS.49.45.

[11] Blakey-Milner, B., Gradl, P., Snedden, G., Brooks, M., Pitot, J., Lopez, E., Leary, M., Berto, F., du Plessis, A. (2021). Metal additive manufacturing in aerospace: A review, Mater. Des., 209, pp. 110008.

[12] Bournias-Varotsis, A., Han, X., Harris, R.A., Engstrøm, D.S. (2019). Ultrasonic additive manufacturing using feedstock with build-in circuitry for 3D metal embedded electronics, Addit. Manuf., 29, pp. 100799.

[13] Fiorentin, F.K., Oliveira, B., Pereira, J.C.R., Correia, J.A.F.O., de Jesus, A.M.P., Berto, F. (2021). Fatigue behaviour of metallic components obtained by topology optimization for additive manufacturing, Frat. Ed Integrita Strutt., 15(55), pp. 119–135, DOI: 10.3221/IGF-ESIS.55.09.

[14] Cucinotta, F., Raffaele, M., Salmeri, F. (2020).A Topology Optimization Method for Stochastic Lattice Structures. International Joint Conference on Mechanics, Design Engineering & Advanced Manufacturing, Springer, pp. 235–240.

[15] Barberi, E., Cucinotta, F., Raffaele, M., Salmeri, F. (2021).A Hollowing Topology Optimization Method for Additive and Traditional Manufacturing Technologies. International Conference on Design, Simulation, Manufacturing: The Innovation Exchange, Springer, pp. 422–430.

[16] Valerga, A.P., Batista, M., Salguero, J., Girot, F. (2018). Influence of PLA filament conditions on characteristics of FDM parts, Materials (Basel)., 11(8), DOI: 10.3390/ma11081322.

[17] Zakeri, S., Vippola, M., Levänen, E. (2020). A comprehensive review of the photopolymerization of ceramic resins used in stereolithography, Addit. Manuf., 35, pp. 101177.

[18] Ferro, P., Romanin, L., Berto, F. (2020). Understanding powder bed fusion additive manufacturing phenomena via numerical simulation, Frat. Ed Integrita Strutt., 14(53), pp. 252–284, DOI: 10.3221/IGF-ESIS.53.21.

[19] Charoo, N.A., Barakh Ali, S.F., Mohamed, E.M., Kuttolamadom, M.A., Ozkan, T., Khan, M.A., Rahman, Z. (2020). Selective laser sintering 3D printing–an overview of the technology and pharmaceutical applications, Drug Dev. Ind. Pharm., 46(6), pp. 869–877.

[20] Epasto, G., Palomba, G., D'Andrea, D., Guglielmino, E., Di Bella, S., Traina, F. (2019). Ti-6Al-4V ELI microlattice structures manufactured by electron beam melting: Effect of unit cell dimensions and morphology on mechanical behaviour, Mater. Sci. Eng. A, 753, pp. 31–41, DOI: 10.1016/j.msea.2019.03.014.
[21] Epasto, G., Palomba, G., Andrea, D.D., Di Bella, S., Mineo, R., Guglielmino, E., Traina, F. (2019).Experimental investigation of rhombic dodecahedron micro-lattice structures manufactured by Electron Beam Melting. Materials Today: Proceedings, 7, pp. 578–585.
[22] Dudek, P. (2013). FDM 3D printing technology in manufacturing composite elements, Arch. Metall. Mater., 58(4), pp. 1415–1418, DOI: 10.2478/amm-2013-0186.
[23] Popescu, D., Zapciu, A., Amza, C., Baciu, F., Marinescu, R. (2018). FDM process parameters influence over the mechanical properties of polymer specimens: A review, Polym. Test., 69, pp. 157–166, DOI: 10.1016/j.polymertesting.2018.05.020.
[24] Chatzidai, N., Karalekas, D. (2019). Experimental and numerical study on the influence of critical 3D printing processing parameters, Frat. Ed Integrita Strutt., 13(50), pp. 407–413, DOI: 10.3221/IGF-ESIS.50.34.
[25] Zhao, Y., Chen, Y., Zhou, Y. (2019). Novel mechanical models of tensile strength and elastic property of FDM AM PLA materials: Experimental and theoretical analyses, Mater. Des., 181, pp. 108089, DOI: 10.1016/j.matdes.2019.108089.
[26] Yao, T., Ye, J., Deng, Z., Zhang, K., Ma, Y., Ouyang, H. (2020). Tensile failure strength and separation angle of FDM 3D printing PLA material: Experimental and theoretical analyses, Compos. Part B Eng., 188, pp. 107894, DOI: 10.1016/j.compositesb.2020.107894.
[27] Djouda, J.M., Gallittelli, D., Zouaoui, M., Makke, A., Gardan, J., Recho, N., Crépin, J. (2020). Local scale fracture characterization of an advanced structured material manufactured by fused deposition modeling in 3D printing, Frat. Ed Integrita Strutt., 14(51), pp. 534–540, DOI: 10.3221/IGF-ESIS.51.40.
[28] Montinaro, N., Cerniglia, D., Pitarresi, G. (2018). A numerical and experimental study through laser thermography for defect detection on metal additive manufactured parts, Frat. Ed Integrita Strutt., 12(43), pp. 231–240, DOI: 10.3221/IGF-ESIS.43.18.
[29] Ricotta, M., Meneghetti, G., Atzori, B., Risitano, G., Risitano, A. (2019). Comparison of Experimental Thermal Methods for the Fatigue Limit Evaluation of a Stainless Steel, Metals (Basel), 9(6), pp. 677, DOI: 10.3390/met9060677.
[30] Corigliano, P., Cucinotta, F., Guglielmino, E., Risitano, G., Santonocito, D. (2020). Fatigue assessment of a marine structural steel and comparison with Thermographic Method and Static Thermographic Method, Fatigue Fract. Eng. Mater. Struct., 43(4), pp. 734–743, DOI: 10.1111/ffe.13158.
[31] Seitl, S., Klusák, J., Fernández, P., Canteli, A. (2014). Thermographic determination methodology: Application on fatigue limit of AL 2024 for R=-1, Key Eng. Mater., 577–578, pp. 477–480, DOI: 10.4028/www.scientific.net/KEM.577-578.477.
[32] Lipski, A. (2016). Accelerated determination of the fatigue limit and the s-n curve by means of the thermographic method for x5crni18-10 steel, Acta Mech. Autom., 10(1), pp. 22–27, DOI: 10.1515/ama-2016-0004.
[33] Risitano, A., Risitano, G. (2013). Determining fatigue limits with thermal analysis of static traction tests, Fatigue Fract. Eng. Mater. Struct., 36(7), pp. 631–639, DOI: 10.1111/ffe.12030.
[34] Wiberg, A., Persson, J., Ölvander, J. (2019). Design for additive manufacturing – a review of available design methods and software, Rapid Prototyp. J., 25(6), pp. 1080–1094, DOI: 10.1108/RPJ-10-2018-0262.
[35] Curti, G., La Rosa, G., Orlando, M., Risitano, A. (1986). Analisi tramite infrarosso termico della temperatura limite in prove di fatica, Proc. XIV Convegno Naz. AIAS, pp. 211–220.
[36] La Rosa, G., Risitano, A. (2000). Thermographic methodology for rapid determination of the fatigue limit of materials and mechanical components, Int. J. Fatigue, 22(1), pp. 65–73, DOI: 10.1016/S0142-1123(99)00088-2.
[37] Fargione, G., Geraci, A., La Rosa, G., Risitano, A. (2002). Rapid determination of the fatigue curve by the thermographic method, Int. J. Fatigue, 24(1), pp. 11–19, DOI: 10.1016/S0142-1123(01)00107-4.
[38] Thomson, W. (1853). XV. On the Dynamical Theory of Heat, with numerical results deduced from Mr Joule's Equivalent of a Thermal Unit, and M. Regnault's Observations on Steam, Trans. R. Soc. Edinburgh, 20(2), pp. 261–288, DOI: 10.1017/S0080456800033172.
[39] Caglioti, G., Ferro Milone, A., Società italiana di fisica. (1982). Mechanical and thermal behaviour of metallic materials : Varenna on Lake Como, Villa Monastero, 30th June - 10th July 1981, North-Holland Pub. Co.
[40] Melvin, A.D., Lucia, A.C., Solomos, G.P., Volta, G., Emmony, D. (1990). Thermal emission measurements from creep damaged specimens of AISI 316L and Alloy 800H, Proc. 9th Int. Conf. Exp. Mech. 2, pp. 765-773.
[41] Melvin, A.D., Lucia, A.C., Solomos, G.P. (1993). The thermal response to deformation to fracture of a carbon/epoxy composite laminate, Compos. Sci. Technol., 46(4), pp. 345–351, DOI: 10.1016/0266-3538(93)90180-O.

[42] Risitano, G., Clienti, C. (2011). Experimental Study to Verify the Fatigue Limit Found by Thermal Analysis of Specimen Surface in Mono Axial Traction Test, Key Eng. Mater., 488–489, pp. 795–798, DOI: 10.4028/www.scientific.net/KEM.488-489.795.
[43] Dawoud, M., Taha, I., Ebeid, S.J. (2016). Mechanical behaviour of ABS: An experimental study using FDM and injection moulding techniques, J. Manuf. Process., 21, pp. 39–45, DOI: 10.1016/j.jmapro.2015.11.002.
[44] Ziemian, C., Sharma, M., Ziemi, S. (2012). Anisotropic Mechanical Properties of ABS Parts Fabricated by Fused Deposition Modelling, Mech. Eng., DOI: 10.5772/34233.
[45] Rodríguez-Panes, A., Claver, J., Camacho, A.M. (2018). The influence of manufacturing parameters on the mechanical behaviour of PLA and ABS pieces manufactured by FDM: A comparative analysis, Materials (Basel)., 11(8), DOI: 10.3390/ma11081333.
[46] Samykano, M., Selvamani, S.K., Kadirgama, K., Ngui, W.K., Kanagaraj, G., Sudhakar, K. (2019). Mechanical property of FDM printed ABS: influence of printing parameters, Int. J. Adv. Manuf. Technol., 102(9–12), pp. 2779–2796, DOI: 10.1007/s00170-019-03313-0.
[47] Srinivasan, R., Ruban, W., Deepanraj, A., Bhuvanesh, R., Bhuvanesh, T. (2020). Effect on infill density on mechanical properties of PETG part fabricated by fused deposition modelling, Mater. Today Proc., 27, pp. 1838–1842, DOI: 10.1016/j.matpr.2020.03.797.
[48] Vergani, L., Colombo, C., Libonati, F. (2014). A review of thermographic techniques for damage investigation in composites, Frat. Ed Integrita Strutt., 8(27), pp. 1–12, DOI: 10.3221/IGF-ESIS.27.01.
[49] Santonocito, D. (2020). Evaluation of fatigue properties of 3D-printed Polyamide-12 by means of energy approach during tensile tests, Procedia Struct. Integr., 25(2019), pp. 355–363, DOI: 10.1016/j.prostr.2020.04.040.
[50] Santonocito, D., Foti, P., Risitano, G., Berto, F. (2021). Fatigue damage assessment in AM polymers evaluating their energy release, Procedia Struct. Integr., 34(2019), pp. 211–220, DOI: 10.1016/j.prostr.2021.12.031.